Edge-Grafted Molecular Junctions between Graphene Nanoplatelets: Applied Chemistry to Enhance Heat Transfer in Nanomaterials

ADVANCED FUNCTIONAL MATERIALS

www.afm-journal.de

# Edge-Grafted Molecular Junctions between Graphene Nanoplatelets: Applied Chemistry to Enhance Heat Transfer in Nanomaterials

*Maria Mar Bernal, Alessandro Di Pierro, Chiara Novara, Fabrizio Giorgis, Bohayra Mortazavi, Guido Saracco, and Alberto Fina**

**The edge-functionalization of graphene nanoplatelets (GnP) is carried out exploiting diazonium chemistry, aiming at the synthesis of edge decorated nanoparticles to be used as building blocks in the preparation of engineered nanostructured materials for enhanced heat transfer. Indeed, both phenol functionalized and dianiline-bridged GnP (GnP-OH and E-GnP, respectively) are assembled in nanopapers exploiting the formation of non-covalent and covalent molecular junctions, respectively. Molecular dynamics allow to estimate the thermal conductance for the two different types of molecular junctions, suggesting a factor 6 between conductance of covalent vs non-covalent junctions. Furthermore, the chemical functionalization is observed to drive the self-organization of the nanoflakes into the nanopapers, leading to a 20% enhancement of the thermal conductivity for GnP-OH and E-GnP while the cross-plane thermal conductivity is boosted by 190% in the case of E-GnP. The application of chemical functionalization to the engineering of contact resistance in nanoparticles networks is therefore validated as a fascinating route for the enhancement of heat exchange efficiency on nanoparticle networks, with great potential impact in low-temperature heat exchange and recovery applications.**

## 1. Introduction

The fast-growing development of modern technologies made efficient heat dissipation extremely important to the performance, lifetime, and reliability of electronic and optoelectronic devices. In this regard, there is an urgent need for the development of flexible and lightweight thermally conductive materials to improve the thermal management efficiency of such systems. Graphene sheets, owing to their exceptional mechanical and electrical properties and high intrinsic thermal conductivity,[1] are of great interest to be used as building blocks to create macroscopic assembled materials with unique properties.[2] While graphene, defined as a single layer $sp^2$ carbon, currently remains of insufficient availability for the use in large scale bulk applications, graphene related materials (GRM), including reduced graphene oxide, few layer graphene, multilayer graphene, and graphene nanoplatelets, represent the state-of-the-art materials for the exploitation into thermally conductive applications. Specifically, large-area freestanding "paper-like" materials made from GRM have emerged as promising materials to address heat dissipation problems in practical applications.[2d,3]

GRM nanopapers show strongly anisotropic thermal conductivity between the in-plane and cross-plane directions,[3c] reflecting the strong covalent $sp^2$ bonding between carbon atoms on graphene sheets, and the weak van der Waals (VdW) interactions between them.[4] Engineering the heat conduction in GRM nanopapers is non-trivial. On the one hand, the thermal conductivity depends on the quality of the individual GRM sheets, i.e., the number of defects per unit area and the aspect ratio, which determine the phonon transmission on the individual nanoflake.[2d,5] Higher concentration of defects such as vacancies, inclusions, stacking defects, oxidized carbons, or other functional groups are indeed well known to restrain the thermal conductivity of the individual nanoflakes.[6] On the other hand, the physico-chemical nature of the contact between the nanoflakes and the extension of the contact area inside the nanopaper determine the thermal contact resistance.[3a,5b,7] Previous experimental and theoretical

Dr. M. Mar Bernal, A. Di Pierro, Prof. A. Fina
Dipartimento di Scienza Applicata e Tecnologia
Politecnico di Torino
Alessandria 15121, Italy
E-mail: alberto.fina@polito.it
Dr. C. Novara, Prof. F. Giorgis, Prof. G. Saracco
Dipartimento di Scienza Applicata e Tecnologia
Politecnico di Torino
Torino 10129, Italy
Dr. B. Mortazavi
Institute of Structural Mechanics
Bauhaus-Universität Weimar
Marienstr. 15, D-99423 Weimar, Germany

The ORCID identification number(s) for the author(s) of this article can be found under https://doi.org/10.1002/adfm.201706954.



**DOI: 10.1002/adfm.201706954**

studies have reported the dependency of the thermal conductivity with the average lateral size of the graphene, indicating that the heat conduction in graphene is limited by the phonon mean free path.[8] However, an increase in the average lateral size of few-layer-graphene flakes was also demonstrated to increase the thermal conductivity of the microlayer deposited on a polymer film, suggesting that the overall conductivity of the network is indeed limited by the contact resistance between the nanoflakes.[5b] It is worth noting that air cavities are typically obtained in the deposition of GRM nanoflakes, owing to the non-planarity of the nanoflakes and/or defects in stacking and orientation. The reduction of the number and total volume of the air cavities in the graphene assemblies obviously enhances the thermal contact between particles, thus improving the overall thermal conductivity.[7b] A simple way to reduce porosity of the deposition and enhance particle–particle contacts is by mechanical compaction via the application of uniaxial pressure on the deposition, which was demonstrated beneficial for the improvement of the thermal conduction.[5b] To maximize the thermal conductivity of graphene nanopapers, annealing at extremely high temperatures is typically carried out on the preformed papers, in order to restore complete $sp^2$ hybridization in the graphene sheets by removing oxidized groups and recombine structural defects[9] or by the formation of new $sp^2$ clusters.[10] Beside the increase in conductivity of the individual nanoflakes,[6a] defectiveness reduction upon thermal annealing may also affect the extent of $\pi$–$\pi$ interactions, finally improving the contact between adjacent nanoflakes. Furthermore, coalescence of overlapped sheets may occur at high annealing temperature, leading to the formation of extended polycrystalline layers.[11] Such approach endows graphene nanopapers with superior thermal conductivities in the in-plane direction but extremely low in the normal direction. Despite this may be fine when only considering heat spread over the nanopapers, the thermal transport along the cross-plane direction remains crucial to guarantee an efficient thermal contact between the GRM paper spreader and the heater and/or the heat sink.

To tailor the properties of nanopapers, the exploitation of molecular junctions between GRM nanoflakes is currently a promising possibility, yet experimentally challenging. In fact, while the conductance of molecular junctions was widely studied by molecular dynamics[12] and density functional theory,[13] the experimental exploitation of organic molecular junctions was only recently reported by Han et al.[14] for the thermal coupling of the graphene–graphene oxide and the graphene oxide–silica surfaces. In this work, both covalent and non-covalent molecular junctions were designed and synthetized to create GRM-based nanopapers with inherently low contact thermal resistance between nanoplatelets. Such molecular junctions were built at the edges of the nanoflakes by means of the controlled diazonium chemistry, allowing to preserve the defect-free $sp^2$ structure, as confirmed by X-ray photoelectron spectroscopy (XPS) and Raman spectroscopy. Enhanced heat transfer performance of the nanopapers was assessed experimentally in both in-plane and cross-plane directions and interpretation of these results was further supported by molecular dynamics and finite-element modeling.

## 2. Results and Discussion

The objective of this study was to manufacture and validate molecular junctions between graphene nanoplatelets for the modulation of the thermal conductivities of GRM networks. In this framework, edge-selective functionalization is of utmost interest to obtain engineered nanoparticles able to further react or assemble in a finely controlled way, while preserving the high conductivity associated with the defect-free $sp^2$ structure of graphene. As a first step towards that target, we investigated the diazonium reaction conditions, to maximize the amount of chemical functions added at the edges of our graphene nanoplatelets (GnP) without affecting the conjugated $\pi$-system. The well-established procedure[15] for the in situ formation of the diazonium species from an anilinic compound, namely 4-aminophenol, in the presence of an alkyl nitrite was followed in this work (**Scheme 1**a; Scheme S1, Supporting Information). Thermogravimetric analysis (TGA), X-ray photoelectron spectroscopy (XPS), and Raman spectroscopy were used to characterize the amount of species attached to GnP (Figure S1, Supporting Information), their chemical composition (Figures S2–S5 and Table S1, Supporting Information), and the microstructure changes of GnP due to the covalent functionalization (Figure S6, Supporting Information). The optimized conditions for the edge-selective functionalization of our GnP using the diazonium chemistry were found to be 4 equiv. per C atom of the anilinic molecule for 24 h of reaction time (GnP-OH). Indeed, at lower concentration the degree of functionalization decreased, while at higher reaction times no improvements on the extent of the reaction were observed while the number of OH groups diminished.

The next step was to edge-link GnP to produce the molecular junction between nanosheets. To do so, 1,5-bis(4-aminophenyloxy)pentane (**3**) was used to establish an equivalent molecular junction in one step (Scheme 1b), by the in situ formation of the diazonium salts of compound **3**, referred to as edge-linked GnP (E-GnP) (Scheme 1b). The reaction was carried out by adapting the optimized diazonium conditions established above for the edge-selective functionalization of our GnP with 4-aminophenol (see the Experimental Section for details).

Evidences on the functionalization of GnP come from the XPS spectroscopic measurements. The high-resolution C1s XPS spectra of the nanoplatelets were deconvoluted into six bands (see the Experimental Section for details). The low oxygen content observed for pristine GnP (1.74 atomic percentage, at%) increased to 5.23% after functionalization with 4-aminophenol. In GnP-OH a clear band at 285.7 eV, not detected in the pristine GnP, corresponding to the C–OH groups (**Figure 1**d) was observed, thus confirming the grafting of phenolic groups to the nanoflakes. On the other hand, in the C1s spectrum of E-GnP (Figure 1f) the band located at ≈286.6 eV corresponding to the C–O–C groups is higher than in GnP-OH, which is a clear evidence of the successful functionalization of GnP in one step by arylation with diazonium salts. Indeed, it can be clearly observed in the O1s spectrum of E-GnP (Figure S7, Supporting Information) that the vast majority of oxygen moieties corresponds to single bonded C–O–C groups.[6a] Furthermore, it is worth noting that the oxygen content is 6.29%, which is higher to that observed in GnP-OH. This confirms that the optimized conditions for the diazonium reaction with 4-aminophenol are

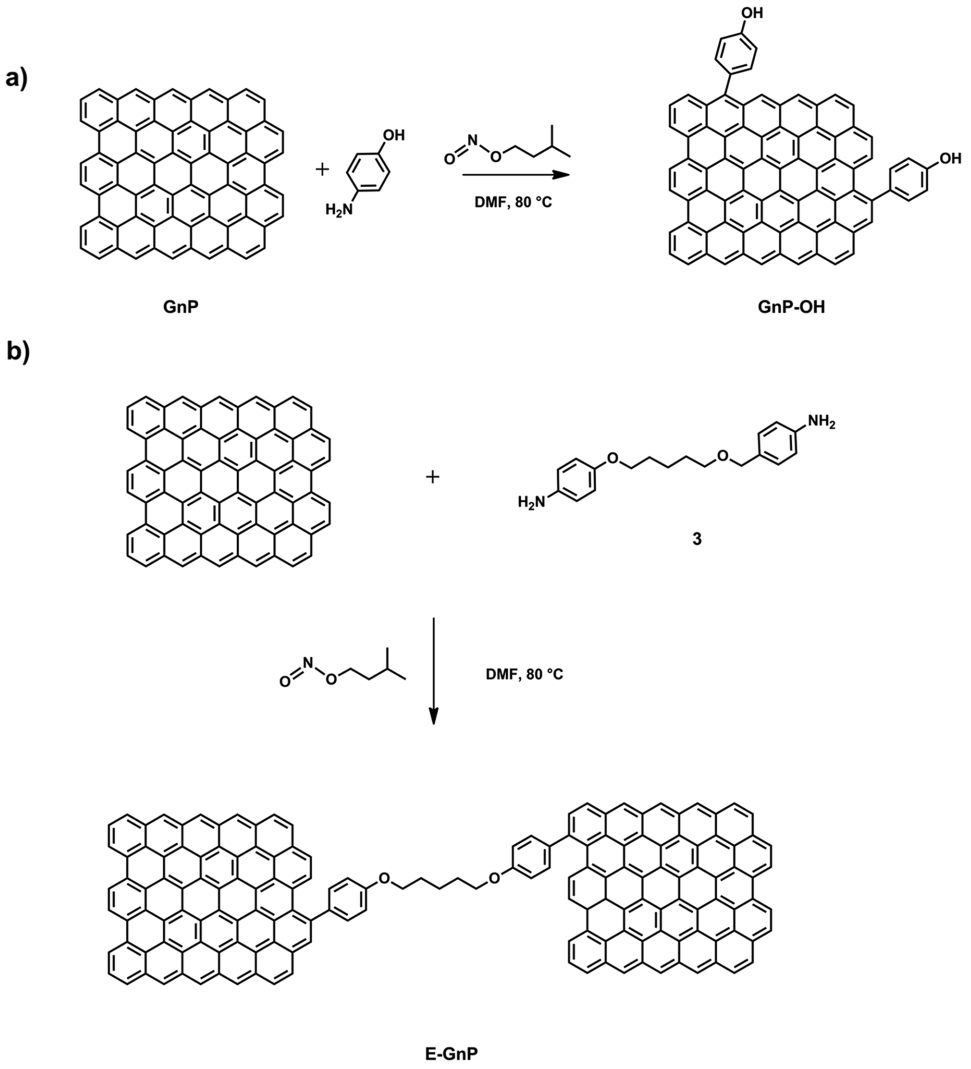


**Scheme 1.** a) Edge-selective functionalization with 4-aminophenol. b) Edge-linked (E-GnP) with 1,5-bis(4-aminophenyloxy)pentane (**3**).

valid also for the dianilinic compound **3**. These observations are confirmed by the values of the at% of each oxygen functional group summarized in Table S2 (Supporting Information) and the bands assigned in the O1s spectra of the graphene nanoplatelets (Figure S7, Supporting Information).

Upon functionalization either by 4-aminophenol (Figure 1c) or compound **3** (Figure 1e), a weak N1s peak was observed on the XPS survey spectra, being N/C ratio 0.04 for both GnP-OH and E-GnP. Analysis of the N1s spectra (Figure S8, Supporting Information) revealed one broad band in the range 398–400 eV, which can be ascribed to amine ($-NH_2$) and/or azo ($-N=N-$) groups.[16] Indeed, the presence of the $NH_2$ groups is attributed to the adsorption of the starting anilinic molecule, while the appearance of the azo groups can be related to the diazonium ion molecules generated in situ that form a charge-transfer complex with the graphene surface.[17]

While the XPS analysis evidences the functionalization of GnP with $-OH$ groups and the latter formation of the ether linkage, this technique provides no information on the location of the functional groups on the GnP flakes. In particular, despite the diazonium functionalization was previously shown to start from the edges of graphene sheets,[18] where the most reactive sites are located, the occurring of the reaction at the edges of GnP was also investigated.

Raman spectroscopy, because of its sensitivity to changes in atomic structures, has proved to be an appropriate technique to characterize the presence of disorder in $sp^2$-hybridized carbon-based systems.[19] In particular, it can determine the nature of disorder, from point defects and boundaries to zig-zag and armchair edges. In this study, Raman spectroscopy was used to obtain evidence of the preferential functionalization of graphene nanoflakes at the edges. The most characteristic peaks in the Raman spectrum of graphene-based materials are the so-called G band (≈1575 $cm^{-1}$) associated with the doubly degenerate in-plane transverse/longitudinal optical phonon modes (i-TO/i-LO); the G′ mode (≈2700 $cm^{-1}$) due to a double resonance intervalley Raman scattering process with two in-plane transverse optical phonons (iTO) at the K point and the D band

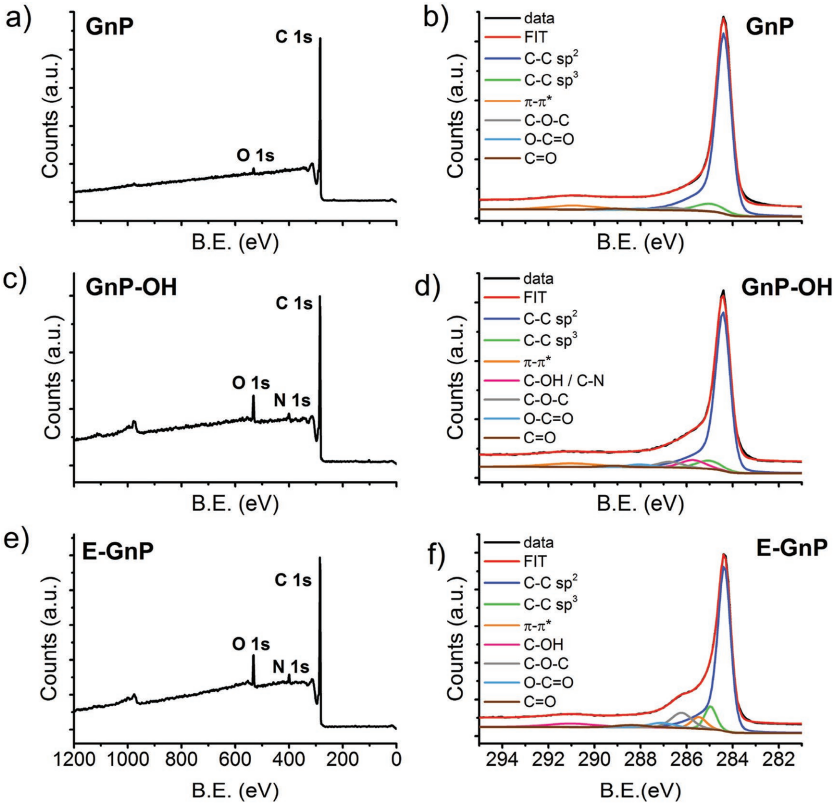


**Figure 1.** Survey XPS spectra and C 1s XPS spectra of a,b) GnP, c,d) GnP-OH, and e,f) E-GnP.

(≈1350 $cm^{-1}$) arising from the iTO phonon mode near K points in the Brillouin zone. The D band is activated by structural defects by a second-order Raman scattering process through the intervalley double resonance and thus its intensity is proportional to the amount of disorder in the sample. Thus, the ratio between the intensities of the D band and the G band ($I_D/I_G$) provides a parameter for quantifying disorder.[19b,20] Spatial mapping of $I_D/I_G$ (**Figure 2**a–c) of the different graphene nanoplatelets was useful to localize the regions with higher defect density. As expected, the $I_D/I_G$ ratio is lower in the basal planes of the unfunctionalized starting material than near the edges (Figure 2a). Upon functionalization to obtain GnP-OH and E-GnP the amount of disorder on the basal planes, observed in the corresponding spatial mappings, did not present major differences if compared to the unfunctionalized GnP, confirming that the grafting procedure does not introduce significant defectiveness in the $sp^2$ structure. However, single-point Raman spectra recorded near the edges and the center regions of the different flakes (Figure 2d–f) revealed an increase of the $I_D/I_G$ ratio at the borders.

The first-order Raman region (up to 2000 $cm^{-1}$) of points localized at the edges of the flakes was well fitted by Lorentzian functions (**Figure 3**). The unfunctionalized GnP shows the characteristic D and G bands, while the second disorder-induced peak around 1614 $cm^{-1}$ (the D′ band) also becomes evident (Figure 3a). In GnP-OH, additional features at 1167, 1210, 1279, 1420, 1495, and 1542 $cm^{-1}$ were observed in the first-order Raman spectral region (Figure 3b). The peak at 1495 $cm^{-1}$ can be assigned to the iTO phonon branch that becomes Raman active by the intravalley double resonance Raman process.[19a,21] The peak at 1167 $cm^{-1}$ coupled with the peak at 1420 $cm^{-1}$ is a signature of *trans*-polyacetylene, as reported by Ferrari et al.[22] On the other hand, the peak at 1210 $cm^{-1}$ and its companion feature at 1542 $cm^{-1}$ have been assigned to *cis*-polyacetylene.[23] *Trans*- and *cis*-polyacetylene present zig-zag and armchair structures similar to the edges of graphene sheets.[24] Then the origin of these two pair of coupled modes, 1167–1420 $cm^{-1}$ and 1210–1542 $cm^{-1}$, was ascribed to C—C and C=C stretching bond vibrations of the edge atoms of graphene flakes, respectively, justified by interrupted conjugation at the edges of graphene sheets. Such interruption of conjugation in the graphene may be obtained as a consequence of grafting at the graphene edges. Clearly, in the reaction condition used, distance between two grafted molecules cannot be controlled and is expected to result in a wide distribution of conjugation length, which appear confirmed by the broad signals observed in the Raman spectra. Similar features were previously reported for edge-carboxylated nanosheets[25] and functionalized graphene with diazonium salts,[26] thus confirming the functionalization at the edges of the flakes. Finally, the observation of the C–O stretching vibrations for *p*-monosubstituted phenol at around 1279 $cm^{-1}$,[27] provides irrefutable evidence of the grafting of phenol groups at the edges of the GnP.

The Raman spectra of E-GnP does not clearly show the presence of the weak coupled bands previously observed in GnP-OH ascribed to interrupted conjugations (armchair and zig-zag structures) of the edges of graphene. Instead, features at 1140 and 1517 $cm^{-1}$ can be clearly observed in the Raman spectrum of E-GnP. Both bands are also observed in the Raman spectrum of the dianilinic compound **3** (Figure S9, Supporting Information), thus further proving grafting in E-GnP.[27a] Furthermore, the Raman mapping of the ratio between the $I_{1140\ cm^{-1}}/I_G$, shown in Figure S10 (Supporting Information), confirms the preferential location of the alkyl chains at the edges of the graphene nanoplatelets. In addition, it is worth noting that the bands in the 1350–1500 $cm^{-1}$ region observed in the anilinic compound, ascribed to C—N bonds, are not detectable in the Raman spectrum of E-GnP,[27a,28] further confirming the covalent grafting of compound **3**.

The effect of edge functionalization on the self-assembly of nanoflakes was investigated by analyzing the size of nanoplatelets deposited from diluted suspensions. Several scanning electron microscopy (SEM) images of GnP, GnP-OH, and E-GnP were analyzed to evaluate the effect of the molecular junctions on the lateral size of the resulting assembly of nanoflakes. Representative SEM images and the corresponding statistical analyses of flakes length are shown in **Figure 4**.

The size analysis of the different nanoflakes (Figure 4d–f) revealed an approximately symmetric distribution of pristine

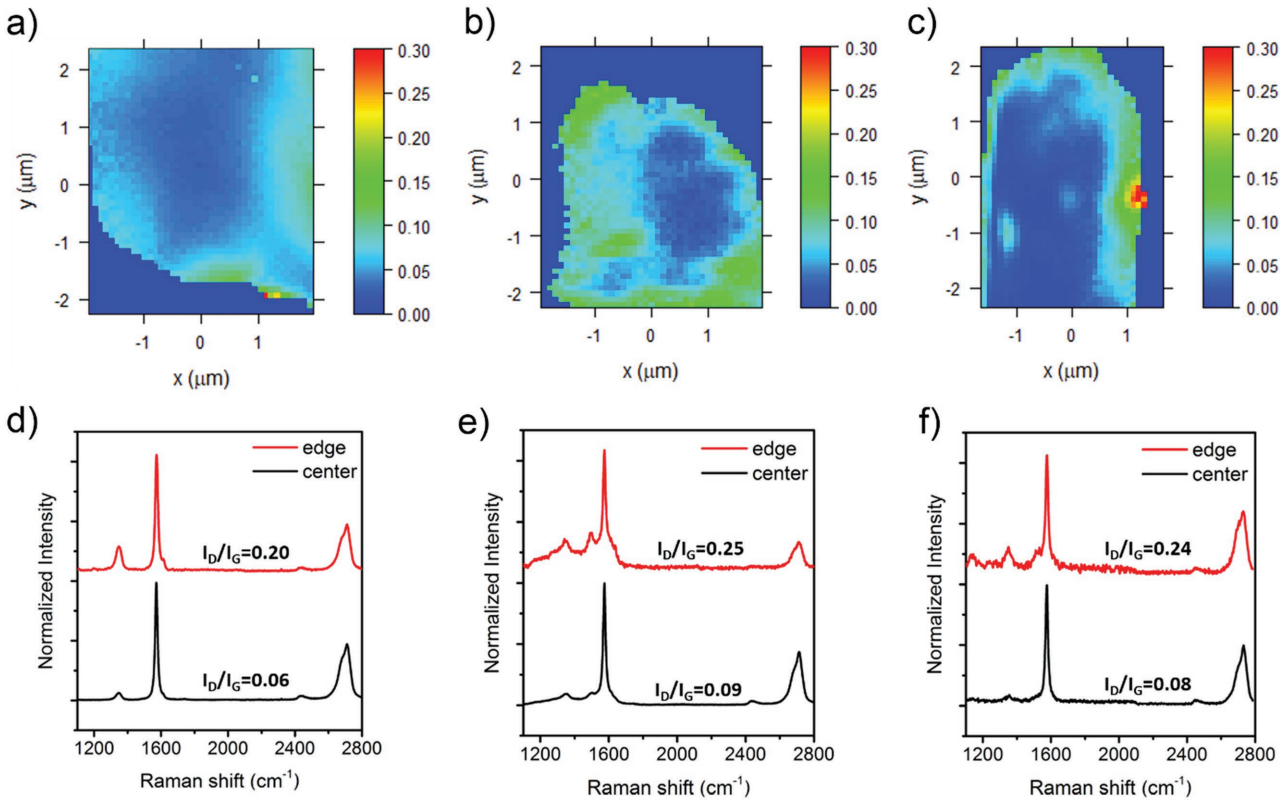


**Figure 2.** Raman mapping of $I_D/I_G$ of a) GnP, b) GnP-OH, and c) E-GnP. d–f) Average Raman spectra extracted from edge and center spots in mappings a–c).

GnP between 1 and 12 µm (D90 = 10 µm), whereas distributions become broader and strongly asymmetric for functionalized GnP. A population of individual nanoflakes, thus sizing in the same range as for pristine GnP, remains well represented in the size distribution for both GnP-OH and E-GnP, suggesting functionalization to be partial and/or inhomogeneous, also including the possibility for dianiline **3** to react on the same nanoflake, i.e., bridging two nearby sites of the same nanoplatelet. However, an additional significant population of assembled nanoflakes were clearly observed for both GnP-OH and E-GnP sizing between 10 and 25 µm, demonstrating the ability of the functionalization to build molecular junctions between the individual nanoflakes. Overall, the size distribution is shifted to larger size, with an increase of D90 to 12 and 13 µm for GnP-OH and E-GnP, respectively. It is worth noting that, while an effective junction may obviously be obtained once dianilinic compound **3** is reacted on two different nanoflakes, the assembly of GnP-OH is ascribed to the formation of secondary interactions via H-bonding between phenolic groups, which were further investigated by Molecular Dynamics (MD).

The effect of chemical functionalization on thermal properties of junctions between nanoflakes was studied by MD calculations on a simplified model system, made of two adjacent graphene sheets edge functionalized with phenols or with the covalent molecular junctions (**Figure 5**), using a well-known method previously reported.[12c]

This method allowed to calculate a 126 pW K$^{-1}$ thermal conductance per single chain in E-GnP, whereas a maximum conductance value of 22 pW K$^{-1}$ was obtained per each couple of edge-grafted interacting phenols, when minimizing the distance between hydroxyl groups. A detailed analysis of the thermal conductance dependence on the distance between nanoribbons is reported in Figures S13 and S14 (Supporting Information). The factor 6 between the conductances for covalent vs non-covalent junctions evidences significant differences on the two functionalization strategies, with a clearly higher thermal transfer efficiency in the presence of covalently bound molecular junctions. Beside the values calculated in idealized junctions, the occurrence of strong coupling between edges of GnP flakes is expected to be beneficial for thermal transfer at the interface in GNP networks, providing additional channels for heat transfer on top of the obvious overlapping of unfunctionalized flakes. As the thermal conductance between parallel overlapping graphene sheets was previously calculated by MD to be 0.38 pW Å$^{-2}$ K$^{-1}$,[12c] it is possible to estimate the heat transfer equivalence of a single covalently bound molecular junction to the conductance obtained when overlapping of two graphene sheets for about 330 Å$^2$, which corresponds to about 130 carbon atoms per layer.

In order to investigate the effect of edge functionalization, graphene nanopapers were prepared by vacuum filtration of suspensions of GnP and functionalized GnP. The free-standing nanopapers were obtained after peeling off from the membrane filter, drying under vacuum, and mechanical pressing. The field emission scanning electron microscopy (FESEM) images of the different nanopapers

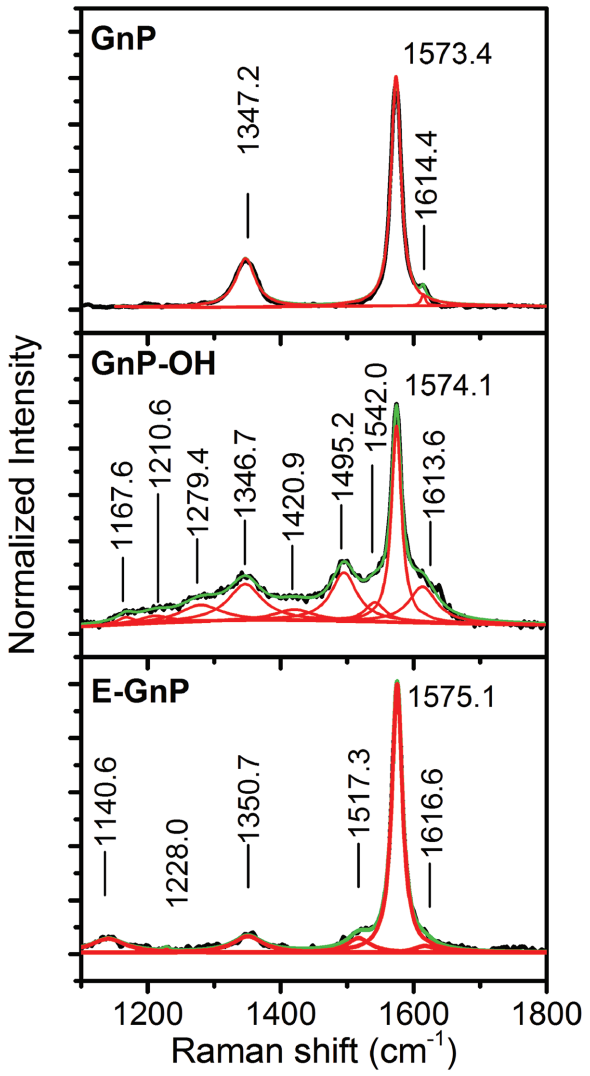


**Figure 3.** First-order Raman spectra recorded from the edges of GnP, GnP-OH, and E-GnP with their deconvolution peaks.

(**Figure 6**) reveal an aligned layered structure through the entire cross-section. As previously reported,[29] the vacuum filtration process produces a degree of order within the structure of the nanopapers, while the morphology of the nanoflakes strongly influences their self-assembly. In our case, the planarity of the starting GnP together with their low defectiveness allows the formation of an ordered and aligned layered structure (Figure 6a,b). However, the density of the nanopaper is about 1.3 g $cm^{-3}$, yielding a porosity of about 41%. In GnP-OH the ordered structure is retained (Figure 6c,d) which is also confirmed by the unmodified density of the nanopaper (Table S3, Supporting Information). E-GnP nanopaper is not as highly aligned as GnP-OH nanopaper and yields a porosity of about 48%. This effect is indeed ascribed to the presence of covalent junctions between different nanoflakes reducing their mobility to organize in a parallel way during filtration.

The thermal conductivity of the graphene nanopapers was calculated from the values of the in-plane ($\alpha_{||}$) and cross-plane ($\alpha_{\perp}$) thermal diffusivities obtained from the light flash measurements (**Table 1**). To take into account the differences in porosity between the different nanopapers, the effect of air on the conductivity of the nanopaper was subtracted using the well-known Maxwell's effective medium approach to calculate the effective conductivity of the GnP network, $k_n$ (see the Experimental Section for details). The values of the in-plane effective network conductivity ($k_{n||}$) were found higher in both GnP-OH (266 W $m^{-1}$ $K^{-1}$) and E-GnP nanopapers (273 W $m^{-1}$ $K^{-1}$), compared to pristine GnP (228 W $m^{-1}$ $K^{-1}$). The increase in thermal conductivity for GnP-OH nanopaper confirms that a strong interaction between the nanoparticles is taking place, explained by the formation of hydrogen bonding. In the case of E-GnP nanopapers, covalent molecular junctions produced between nanoflakes account for a similar value of $k_{n||}$ to that observed in GnP-OH, evidencing the effectiveness of the organic functionalization to mediate thermal transfer between nanoflakes. As expected, the values of the $k_{n\perp}$ are significantly lower compared to those of the $k_{n||}$, thus indicating the high anisotropy of the graphene nanopapers. Beside the absolute values, it is worth noting the $k_{n\perp}$ for functionalized GnP follows a totally different trend respect to the $k_{n||}$. Indeed, the $k_{n\perp}$ is reduced by 35% in GnP-OH nanopaper, while $k_{n\perp}$ of E-GnP nanopapers is 190% higher compared to pristine GnP nanopaper. Such dramatic differences are ascribed to the interactions driving self-assembly and orientation of the nanoflakes in the nanopapers. Indeed, while GnP-OH organizes in highly aligned nanopaper perpendicular to the direction of the filtration flow, thus favoring $k_{n||}$, the presence of grafted phenols may hinder to some extent the vertical stacking of nanoflakes, thus reducing the efficiency of heat transfer in the through-plane direction. On the other hand, in the presence of covalent molecular junctions, the lower orientation observed contributes in increasing the through-plane conduction. Besides the obvious effect of orientation, these results suggest an interplay between the formation of molecular junctions and GnP stacking, i.e., between conduction though molecular bridges versus by $\pi$–$\pi$ overlapping.

In order to compute the cumulative effect of $\pi$–$\pi$ interactions and molecular junctions into a value of thermal conductance, heat transfer was simulated by finite-element method on model nanopapers designed to match both nanoflakes size distribution and nanopaper density, as detailed in the Experimental Section. As a result of the applied heat flux, a steady-state temperature profile establishes along the constructed sample (**Figure 7**).

Based on our modeling results, the interfacial thermal conductance was calculated to be 17, 19, and 26 MW $m^{-2}$ $K^{-1}$ for the GnP, GnP-OH, and E-GnP graphene laminate samples, respectively. These values account for both heat transfer of $\pi$–$\pi$ interactions and molecular junctions, thus providing a cumulative evaluation of the efficiency of thermal contact between the nanoparticles. The results obtained confirm that both covalent and non-covalent molecular junctions are indeed beneficial in improving thermal contacts compared to pristine GnP, with a clearly higher success of covalently bound junctions. The higher efficiency of the covalent molecular junction was finally confirmed by a simple proof-of-concept heat spreader demonstrator (see the Supporting Information), especially in the through-plane direction (Figure S16b, Supporting Information), corroborating the results obtained from the light flash analysis (LFA) technique.

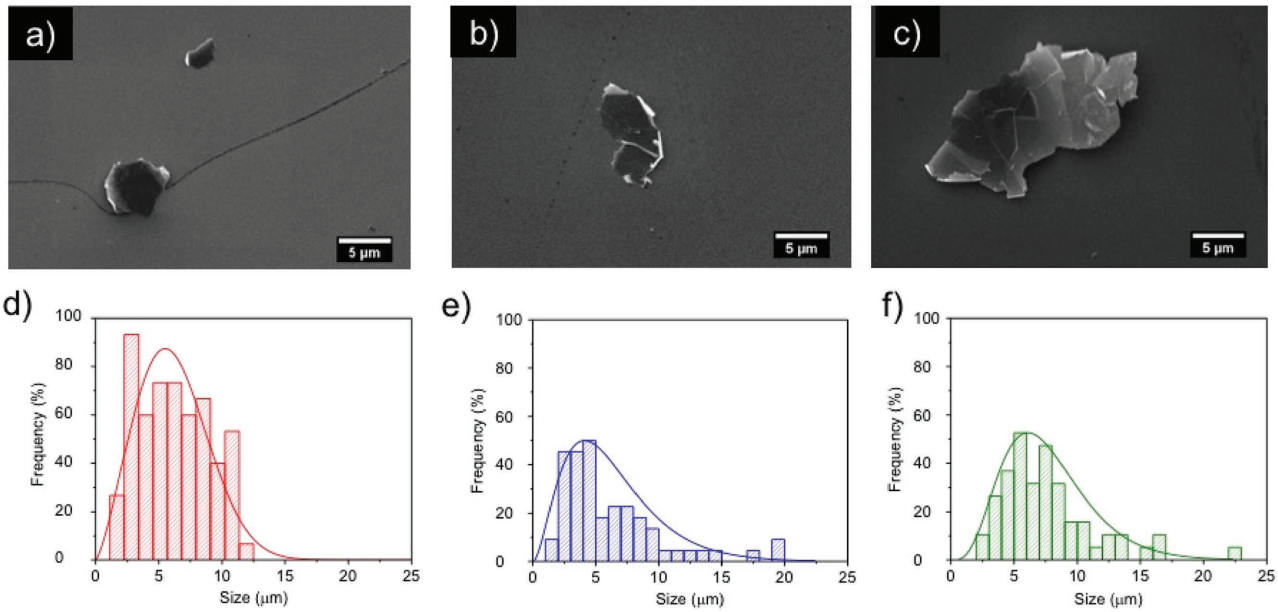


**Figure 4.** SEM images of a) GnP, b) GnP-OH, and c) E-GnP after drop deposition on $SiO_2$/Si substrates and size (maximum length) distribution of the nanoflakes for d) GnP, e) GnP-OH, and f) E-GnP.

## 3. Conclusions

The functionalization of graphite nanoplatelets was obtained via diazonium reaction with either aminophenol or a bifunctional dianilinic compound synthesized on purpose. In both cases, successful covalent grafting was confirmed by XPS, particularly by the strong increase of C–OH and C–O–C signals, respectively. Furthermore, Raman spectroscopy and mapping allowed to prove the preferential location of functional groups at the edges of nanoflakes, allowing to obtain nanoplatelets that are edge decorated with chemical functions suitable for the controlled self-organization into advanced nanomaterials. In particular, the edge functionalization obtained were found suitable to produce molecular junctions between nanoflakes for the enhancement of their thermal boundary conductance. Molecular dynamics investigation suggested a sixfold higher conductance of the covalent molecular junctions designed in this work, compared to the secondary interaction between edge-grafted phenolic groups. Beside the theoretical calculations, experimental evidences of the enhancement in heat transfer

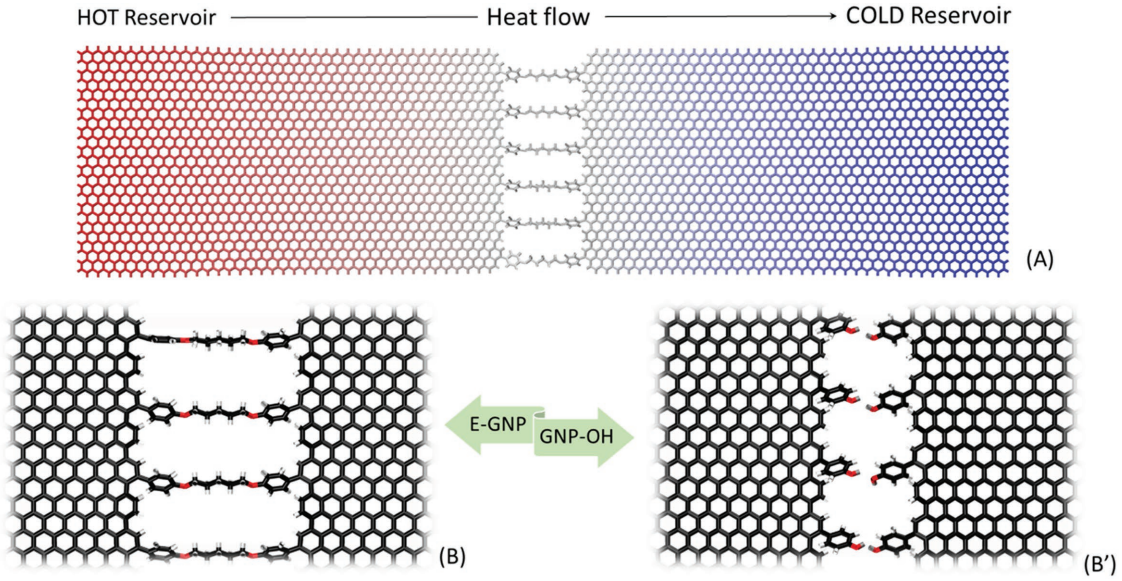


**Figure 5.** Atomistic models for the calculation of thermal conductance. A) Full size model for E-GnP. B,B′) Magnification of representative screenshots from MD simulations for E-GnP and GnP-OH, respectively.

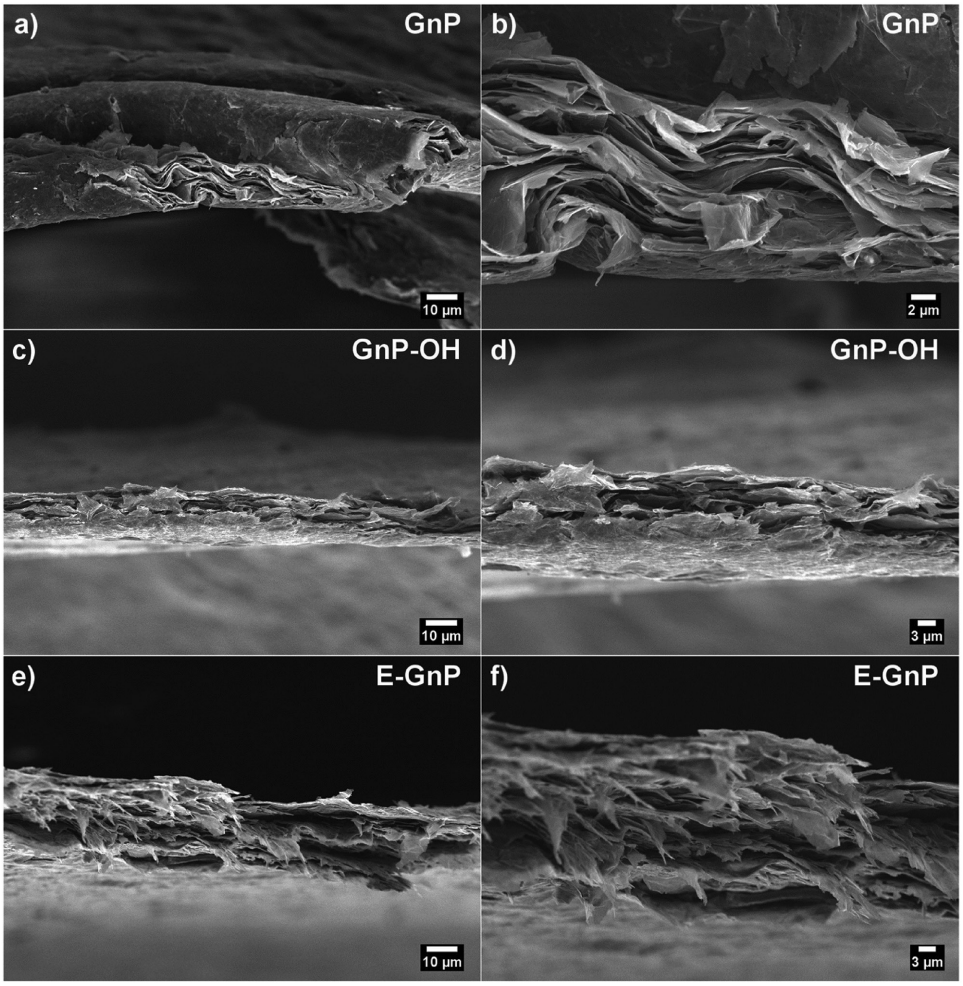


**Figure 6.** Cross-sectional FESEM image of a) GnP, c) GnP-OH, and e) E-GnP and b,d,f) the corresponding higher magnifications, respectively.

were obtained from the thermal characterization of nanopapers prepared by vacuum assisted filtration using the two different functionalized GnP, compared to nanopapers made of pristine GnP. In particular, GnP-OH were used to produce non-covalent molecular junctions between nanoflakes, driven by hydrogen bonding between phenolic groups, while covalent molecular junctions were achieved using E-GnP. Both GnP-OH and E-GnP were demonstrated to enhance the in-plane thermal conductivity by about 20%, while the cross-plane thermal conductivity was dramatically enhanced by 190% in the case of E-GnP. These noticeable enhancements are clearly driven by the GnP functionalization, affecting both the self-assembly and orientation of the nanoflakes in the nanopapers. Indeed, while GnP-OH organizes in highly aligned nanopaper perpendicular to the direction of the filtration flow, the presence of covalent molecular junctions reduced nanoflakes orientation, contributing to the increase of the through-plane heat transfer. The overall enhancement of nanopaper conductivity is therefore associated with an interplay of heat transfer onto molecular junctions and secondary effects related to the different organization of nanoflakes, in terms of orientation and $\pi$–$\pi$ stacking. The chemistry-controlled organization of nanoparticles was therefore validated as a fascinating route for the design and manufacturing of efficient nanomaterials for heat management, including applications as heat spreaders in electronics, as well as in low-temperature heat exchange and heat recovery, currently of utmost interest for the energy efficiency of both industrial and household systems. Beside the thermal conductivity discussed in this paper, the presence of molecular junctions may also play an important role in reducing brittleness of nanopapers, which is typically limiting the exploitation of carbon papers toward the substitution of aluminum or copper foils. Furthermore, the use of molecular junctions between nanoflakes may also

**Table 1.** In-plane ($\alpha_{||}$) and cross-plane ($\alpha_{\perp}$) thermal diffusivities and in-plane ($k_{n||}$) and cross-plane ($k_{n\perp}$) effective thermal conductivities of graphene nanopapers.

| Nanopaper | $\alpha_{\|\|}$ [mm$^2$ s$^{-1}$] | $\alpha_{\perp}$ [mm$^2$ s$^{-1}$] | $k_{n\|\|}$ [W m$^{-1}$ K$^{-1}$] | $k_{n\perp}$ [W m$^{-1}$ K$^{-1}$] |
|---|---|---|---|---|
| GnP | 121.4 ± 1.1 | 0.14 ± 0.01 | 228.4 ± 2.5 | 0.231 ± 0.001 |
| GnP-OH | 141.4 ± 4.5 | 0.10 ± 0.01 | 265.8 ± 9.8 | 0.151 ± 0.001 |
| E-GnP | 141.0 ± 2.5 | 0.37 ± 0.01 | 273.1 ± 5.8 | 0.672 ± 0.001 |

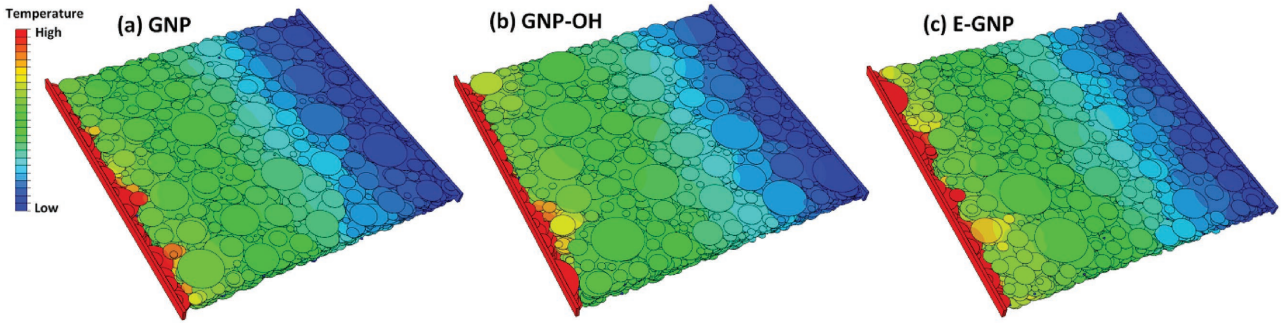


**Figure 7.** In plane temperature profile on nanopapers based on GnP, GnP-OH and E-GnP, from finite-element analysis.

be envisaged for the exploitation in other interface-controlled functional properties of nanopapers, including sensing to chemical or physical conditions affecting the properties of the junctions.

## 4. Experimental Section

All chemical reagents were purchased from Aldrich, Alfa Aesar, Fisher, or Acros Organics and used without further purification unless otherwise stated. Graphene nanoplatelets (G2Nan grade, lateral size ≈10–50 µm and flake thickness ≈10 nm, 99.9%) were kindly supplied by Nanesa (I).

*Edge-Selective Functionalization of GnP with 4-Aminophenol (GnP-OH)*: GnP were first dispersed in *N*,*N*-dimethylformamide (DMF) at a concentration of 1 mg $mL^{-1}$ and sonicated in an ultrasonic bath (maximum operating power 320 W) for 30 min while $N_2$ is bubbled in the suspension. Then, 4-aminophenol was added to the dispersion and the mixture was sonicated for further 15 min under $N_2$ to achieve a homogeneous suspension. After that, isopentyl nitrite (6 equiv. per carbon atom) was slowly added to the dispersion and the temperature of the reaction mixture was raised to 80 °C. The reaction was performed under different conditions (Scheme S1, Supporting Information). After cooling to room temperature, the reaction was quenched into distilled water and filtered through a polytetrafluoroethylene (PTFE) membrane (0.2 µm, Whatman). The filtered cake was redispersed in DMF, sonicated in an ultrasonication bath for 10 min, and filtered through a PTFE membrane (0.2 µm). This sequence was repeated twice with DMF, distilled water, methanol, and diethyl ether. The resulting solids were dried at 80 °C for 24 h.

*Covalently Linked E-GnP*: GnP were first dispersed in DMF at a concentration of 1 mg $mL^{-1}$ and sonicated in an ultrasonic bath (maximum operating power 320 W) for 30 min while $N_2$ is bubbled in the suspension. Then, compound **3** was added to the dispersion and the mixture was sonicated for further 15 min under $N_2$ to achieve a homogeneous suspension. After that, isopentyl nitrite (6 equiv. per carbon atom) was slowly added to the dispersion and the temperature of the reaction mixture was raised to 80 °C. After cooling to room temperature, the reaction was quenched into distilled water and filtered through a PTFE membrane (0.2 µm, Whatman). The filtered cake was redispersed in DMF, sonicated in an ultrasonication bath for 10 min, and filtered through a PTFE membrane (0.2 µm). This sequence was repeated twice with DMF, distilled water, methanol, and diethyl ether. The resulting solids were dried at 80 °C for 24 h.

*Nanopaper Preparation*: GnP and functionalized GnP were suspended in DMF at concentrations of 0.15 mg $mL^{-1}$ and the solutions were sonicated in pulsed mode (15 s on and 15 s off) for 15 min with power set at 30% of the full output power (750 W) by using an ultrasonication probe (Sonics Vibracell VCX-750, Sonics & Materials Inc.) with a 13 mm diameter Ti-alloy tip. The suspensions were subjected to vacuum filtration using a Nylon Supported membrane (0.45 µm nominal pore size, diameter 47 mm, Whatman). After filtration, the as-obtained papers were peeled off from the membranes and dried at 65 °C under vacuum for 2 h to completely remove the solvent. Then, the graphene nanopapers were mechanically pressed in a laboratory hydraulic press (Specac Atlas 15T) under a uniaxial compressive load of 5 kN for 10 min at 25 °C. The density ($\rho$) of the samples was calculated according to the formula $\rho = m/V$, where $m$ is the mass of the nanopaper, weighed using a microbalance (sensitivity: <0.1 µg), and $V$ is calculated from a well-defined disk film using the average thicknesses measured as described in the literature.[30]

*Characterization Methods*: XPS were performed on a VersaProbe5000 Physical Electronics X-ray photoelectron spectrometer with a monochromatic Al source and a hemispherical analyser. Survey scans and high-resolution spectra were recorded with a spot size of 100 µm. The samples were prepared by depositing the GnP powders onto adhesive tape and keeping them under vacuum for 15 h prior to the measurement to remove adsorbed molecules. A Shirley background function was employed to adjust the background of the spectra. Atomic ratios (at%) were calculated from experimental intensity ratios and normalized by atomic sensitivity factors (carbon 0.25, oxygen 0.66, and nitrogen 0.42). The C1s peak was fitted considering the contribution of C—C bond $sp^2$-like using an asymmetric peak (Doniach-Šunjić shape),[31] previously calculated on freshly cleaved highly oriented pyrolytic graphite (HOPG) (ZYH grade, Mikromasch), obtained asymmetry index ($\alpha$) 0.115. The curve fitting was performed using a Gaussian (80%)–Lorentzian (20%) peak shape by minimizing the total square-error fit. The full width at half-maximum (FWHM) of each peak was maintained between 1.3 and 1.4 eV. The C1s spectra is deconvoluted into several peaks: C–C $sp^2$ with binding energy at 284.4 ± 0.1 eV, C–C $sp^3$ at 285.0 ± 0.1 eV, C–OH at 285.7 ± 0.1 eV, C–O–C at 286.6 ± 0.2 eV, O—C=O at 288.0 ± 0.1 eV, C=O at 289.0 ± 0.1 eV, and $\pi$–$\pi^*$ shake-up satellite peak from the $sp^2$-hybridized C atoms at 291.0 ± 0.2 eV.[6a,11,32]

Raman spectroscopy measurements were performed exciting the GnP samples with a 514.5 nm laser coupled to a Renishaw inVia Reflex (Renishaw PLC, United Kingdom) microRaman spectrophotometer. A long working distance 100× objective was employed for the acquisition in backscattering configuration using a laser power of 2.5 mW and an integration time of 15 s. The spectral resolution was 3 $cm^{-1}$. Raman maps were collected after drop deposition from the suspensions of nanoplatelets and drying of the GnP flakes on $SiO_2$/Si substrates with a 100 nm step over a grid including the selected flake area.

Size analysis was carried out by measuring the lateral size of nanoflakes from scanning electron microscopy images. Samples were prepared by depositing ≈10 µL of the suspensions of nanoplatelets on $SiO_2$/Si and dried under inert atmosphere. The images were acquired using an LEO-1450VP Scanning Electron Microscope (beam voltage: 20 kV) and the measurements were performed using ImageJ software (U. S. National Institutes of Health, Maryland, USA, https://imagej.nih.gov/ij/, 1997–2016). Statistical analysis was carried out over ≈75 nanoflakes for each sample, where D90 is the *D*-value (describing particle size distribution) that intercepts at 90% of the cumulative number of particles.

The morphology of the graphene nanopapers was characterized by a high-resolution field emission scanning electron microscope (ZEISS MERLIN 4248).

The in-plane thermal diffusivity ($\alpha_{||}$) and cross-plane diffusivity ($\alpha_{\perp}$) were measured using the xenon light flash (Netzsch LFA 467 *Hyperflash*). The samples were cut in disks of 23 mm with thicknesses between 10 and 30 µm and the measurement of the $\alpha_{||}$ was carried out in a special in-plane sample holder while the $\alpha_{\perp}$ was measured in the standard cross-plane configuration. Each sample was measured five times at 25 °C.

The in-plane and cross-plane thermal conductivities of the nanopapers, $k_{||}$ and $k_{\perp}$ respectively, were then calculated from the equation $k = \rho\alpha C_p$, where $\rho$ is the density of the graphene film and $C_p$ is the specific heat capacity of graphite ($C_p$ = 0.71 J (g K)$^{-1}$). In order to properly take into account the differences and porosity between the different nanopapers, the effect of air was subtracted assuming the nanopaper as a composite in which the continuous matrix is made of GnP particles and the inclusion is air. On such a composite, the well-known Maxwell's effective medium approach was applied (both in-plane and cross-plane) to calculate the effective conductivity of the continuous phase, i.e. the network of nanoflakes, $k_n$, from Equation (1), where $k$ is the thermal conductivity of the nanopaper and $k_{air}$ is the thermal conductivity of air

$$k = k_n \frac{k_{air} + 2k_n + 2\varphi(k_{air} - k_n)}{k_{air} + 2k_n - \varphi(k_{air} - k_n)} \quad (1)$$

*Computational Methods*: Classical molecular dynamics calculations was carried out on LAMMPS (Large-scale Atomistic Molecular Massively Parallel Simulator) package code which implements Velocity Verlet as integration algorithm to recalculate positions and velocities of the atoms. The class II COMPASS force field was adopted in this work, and its functional forms are described by Sun.[33]

The model was composed by two graphene nanoribbons (about 100 Å × 50 Å) connected through the armchair edge by grafted molecules as depicted in Figure 4. The secondary interaction between phenols in GnP-OH were defined by the sum of the VdW contribution from the built-in Lennard Jones 9–6 function and the electrostatic interaction, represented by atomic partial charges.[33] Qeq-equilibration[34] of atomic partial charges was set up in model design.

Grafting density was kept constant at one grafted molecule per couple of aromatic rings on the edge, yielding a total of six grafted molecules on the width of the graphene sheet. The equilibrium distance between the GnP-OH sheets was varied in the range 7.9–15.0 Å and eventually adjusted to 12.5 Å at which the distance between OH groups was minimum, i.e., energy of the secondary interaction was maximum. Details are reported in the Supporting Information. Linear conformation of chains in E-GnP was considered, yielding a 19.6 Å equilibrium distance between graphene sheets. Fully periodic conditions (no replicates) were used along *X* (length), *Y* (width), and *Z* (height). Non Equilibrium Molecular Dynamics (NEMD) calculations were carried out applying Nosé–Hoover thermostats at the ends of the simulation box, i.e., the 10 Å graphene sheets ends. The hot (310 K) and the cold bath (290 K) of the thermostats regions were set as NVT canonical ensemble (constant number of atoms, volume, and temperature) while the region between the two thermostats was set under NVE (constant number of atoms, volume, and energy) condition.

All the simulations were carried out for 15 million time steps (0.25 fs/ts), with an initial 500 kts NVE equilibrium at 300 K and 1 Mts thermostated preheating, followed with the purpose to reach a constant heat flux. After those initial stages, the constant energy flowing through the thermostats started recording. The thermal flow inside NVE regions is calculated from the slope of energy versus time plots.

Temperature profile along the system was calculated by virtually splitting the simulation box transversally into 22 thermal layers. The temperature of each thermal layer was computed by Equation (2), where $T_i$(slab) is the temperature of *i*th slab, $N_i$ is the number of atoms in *i*th slab, $k_B$ is the Boltzmann's constant, and $m_j$ and $p_j$ are atomic mass and momentum of atom *j*, respectively

$$T_i(\text{slab}) = \frac{2}{3N_i k_B} \sum_j \frac{p_j^2}{2m_j} \quad (2)$$

Temperatures were time-averaged to the simulation runtime excluding the non-linear regions at the interfaces, i.e., both close to the thermostats and across the junction.

Single chain thermal conductance $G_s$ expressed in pW K$^{-1}$ has been calculated by Equation (3), where $q_x$ is the thermal flow derived from the energy versus time plot slope, 6 is the number of chains, and $\Delta T$ is the temperature difference across the jump, as projection of the two linear fit of the temperature–length graph in the junction middle point

$$G_s = \frac{q_x}{6 \cdot \Delta T} \quad (3)$$

Finite-element modeling in this study was conducted using the Abaqus/Standard (Version 6.14) package along with the python scripting. As a common assumption, individual GnP were modeled using the disc geometry. Moreover, in agreement with experimental samples we randomly distributed GnP in a way that exactly satisfies the experimentally measured size distributions and porosity of the nanopapers. In our modeling, we constructed relatively large samples including over 4500 individual GnP flakes stacked in 25 layers up together. The thermal conductivity of multilayer graphene was assumed to be 1300 W mK$^{-1}$, according to the experimental measurements by Ghosh et al.[35] We remind that in the graphene laminates the heat percolates not only through the particles but primarily through the contacting surfaces between individual particles. To simulate such a phenomenon, we introduced contact elements between every two contacting flakes with a constant interfacial thermal conductance. For the evaluation of effective thermal conductivity, we included two highly conductive strips at the two ends of the constructed samples that were thermally tied to the graphene flakes.[36] We then applied a constant inward and outward surface heat flux ($q$) on the external surfaces of the included strips. As a result of applied heat flux, a steady-state temperature profile establishes along the constructed sample. The established temperature difference along the laminate, $\Delta T$, was then used to acquire the effective thermal conductivity, $k_{eff}$, using 1D form of the Fourier law (Equation (4))

$$k_{eff} = q \frac{L}{\Delta T} \quad (4)$$

Here, $q$ is the applied heat flux and $L$ is the laminate length (excluding the attached strips). After constructing the finite-element models, we varied the interfacial thermal conductance between the graphene flakes to match the modeling results for the effective thermal conductivity with experimental measurements.

## Supporting Information

Supporting Information is available from the Wiley Online Library or from the author.

## Acknowledgements

This work has received funding from the European Research Council (ERC) under the European Union's Horizon 2020 research and innovation programme under grant agreement 639495—INTHERM—ERC-2014-STG. A limited part of this work was funded by the EU H2020 project Graphene Flagship Core 1, grant agreement no. 696656. B.M. acknowledges the financial support by European Research Council for COMBAT project (Grant number 615132). The authors gratefully acknowledge Francesco Bertocchi at Nanesa (I) for providing GnP, Mauro Raimondo, Giusi Iacono, and Salvatore Guastella at Politecnico di Torino-DISAT for Electron microscopy and XPS analyses. Fabio Carniato

at Università del Piemonte Orientale (I) is gratefully acknowledged for NMR measurements as well as Fausto Franchini at Politecnico di Torino-DISAT for his precious assistance in the heat spreader demonstrator setup and measurements.

A.F. conceived this research work and the experiments within, interpreted the experimental and computational results, and led the research activities. M.M.B. carried out the entire chemical functionalization and nanopaper preparation, performed most of the characterization/data analysis, and participated to interpretation of results. A. DP. carried out MD simulations and postprocessing, under the guidance of B.M. C.N. performed Raman characterization and interpretation with F.G. FEM modeling was conceived and carried out with related analysis by B.M., and G.S. contributed to the discussion of the results. This manuscript was mainly written by M.M.B. and A.F.

## Conflict of Interest

The authors declare no conflict of interest.

## Keywords

edge-selective functionalization, graphene nanoplatelets, molecular dynamics, molecular junctions, thermal conductivity

Received: November 30, 2017
Revised: December 29, 2017
Published online: January 25, 2018

[1] a) C. Gómez-Navarro, R. T. Weitz, A. M. Bittner, M. Scolari, A. Mews, M. Burghard, K. Kern, *Nano Lett.* **2007**, *7*, 3499; b) C. Lee, X. Wei, J. W. Kysar, J. Hone, *Science* **2008**, *321*, 385; c) A. A. Balandin, S. Ghosh, W. Bao, I. Calizo, D. Teweldebrhan, F. Miao, C. N. Lau, *Nano Lett.* **2008**, *8*, 902; d) A. A. Balandin, D. L. Nika, *Mater. Today* **2012**, *15*, 266; e) C. Gómez-Navarro, M. Burghard, K. Kern, *Nano Lett.* **2008**, *8*, 2045.

[2] a) T. Gong, D. V. Lam, R. Liu, S. Won, Y. Hwangbo, S. Kwon, J. Kim, K. Sun, J.-H. Kim, S.-M. Lee, C. Lee, *Adv. Funct. Mater.* **2015**, *25*, 3756; b) D. Li, M. B. Muller, S. Gilje, R. B. Kaner, G. G. Wallace, *Nat. Nanotechnol.* **2008**, *3*, 101; c) X. Lin, X. Shen, Q. Zheng, N. Yousefi, L. Ye, Y.-W. Mai, J.-K. Kim, *ACS Nano* **2012**, *6*, 10708; d) G. Xin, H. Sun, T. Hu, H. R. Fard, X. Sun, N. Koratkar, T. Borca-Tasciuc, J. Lian, *Adv. Mater.* **2014**, *26*, 4521.

[3] a) B. Shen, W. Zhai, W. Zheng, *Adv. Funct. Mater.* **2014**, *24*, 4542; b) N.-J. Song, C.-M. Chen, C. Lu, Z. Liu, Q.-Q. Kong, R. Cai, *J. Mater. Chem. A* **2014**, *2*, 16563; c) J. D. Renteria, S. Ramirez, H. Malekpour, B. Alonso, A. Centeno, A. Zurutuza, A. I. Cocemasov, D. L. Nika, A. A. Balandin, *Adv. Funct. Mater.* **2015**, *25*, 4664.

[4] E. Pop, V. Varshney, A. K. Roy, *MRS Bull.* **2012**, *37*, 1273.

[5] a) W. Feng, M. Qin, Y. Feng, *Carbon* **2016**, *109*, 575; b) H. Malekpour, K. H. Chang, J. C. Chen, C. Y. Lu, D. L. Nika, K. S. Novoselov, A. A. Balandin, *Nano Lett.* **2014**, *14*, 5155.

[6] a) M. Tortello, S. Colonna, M. Bernal, J. Gomez, M. Pavese, C. Novara, F. Giorgis, M. Maggio, G. Guerra, G. Saracco, R. S. Gonnelli, A. Fina, *Carbon* **2016**, *109*, 390; b) B. Mortazavi, S. Ahzi, *Carbon* **2013**, *63*, 460; c) P. A. Denis, F. Iribarne, *J. Phys. Chem. C* **2013**, *117*, 19048; d) A. H. Castro Neto, F. Guinea, N. M. R. Peres, K. S. Novoselov, A. K. Geim, *Rev. Mod. Phys.* **2009**, *81*, 109.

[7] a) P. Kumar, F. Shahzad, S. Yu, S. M. Hong, Y.-H. Kim, C. M. Koo, *Carbon* **2015**, *94*, 494; b) J. Xiang, L. T. Drzal, *Carbon* **2011**, *49*, 773.

[8] a) D. L. Nika, A. S. Askerov, A. A. Balandin, *Nano Lett.* **2012**, *12*, 3238; b) H. Zhang, C. Hua, D. Ding, A. J. Minnich, *Sci. Rep.* **2015**, *5*, 9121; c) G. Fugallo, A. Cepellotti, L. Paulatto, M. Lazzeri, N. Marzari, F. Mauri, *Nano Lett.* **2014**, *14*, 6109.

[9] a) C. Vallés, J. David Núñez, A. M. Benito, W. K. Maser, *Carbon* **2012**, *50*, 835; b) M. M. Bernal, M. Tortello, S. Colonna, G. Saracco, A. Fina, *Nanomaterials* **2017**, *7*, 428.

[10] C. Mattevi, G. Eda, S. Agnoli, S. Miller, K. A. Mkhoyan, O. Celik, D. Mastrogiovanni, G. Granozzi, E. Garfunkel, M. Chhowalla, *Adv. Funct. Mater.* **2009**, *19*, 2577.

[11] R. Rozada, J. I. Paredes, S. Villar-Rodil, A. Martínez-Alonso, J. M. D. Tascón, *Nano Res.* **2013**, *6*, 216.

[12] a) Y. Gao, F. Müller-Plathe, *J. Phys. Chem. B* **2016**, *120*, 1336; b) X. Liu, G. Zhang, Y.-W. Zhang, *J. Phys. Chem. C* **2014**, *118*, 12541; c) A. Di Pierro, G. Saracco, A. Fina, *Comput. Mater. Sci.* **2017**.

[13] a) Q. Li, I. Duchemin, S. Xiong, G. C. Solomon, D. Donadio, *J. Phys. Chem. C* **2015**, *119*, 24636; b) Q. Li, M. Strange, I. Duchemin, D. Donadio, G. C. Solomon, *J. Phys. Chem. C* **2017**, *121*, 7175; c) M. Famili, I. Grace, H. Sadeghi, C. J. Lambert, *ChemPhysChem* **2017**, *18*, 1234; d) L. Medrano Sandonas, R. Gutierrez, A. Pecchia, A. Dianat, G. Cuniberti, *J. Self-Assem. Mol. Electron.* **2015**, *3*, 1.

[14] H. Han, Y. Zhang, N. Wang, M. K. Samani, Y. Ni, Z. Y. Mijbil, M. Edwards, S. Xiong, K. Sääskilahti, M. Murugesan, Y. Fu, L. Ye, H. Sadeghi, S. Bailey, Y. A. Kosevich, C. J. Lambert, J. Liu, S. Volz, *Nat. Commun.* **2016**, *7*, 11281.

[15] Z. Sun, S.-i. Kohama, Z. Zhang, J. R. Lomeda, J. M. Tour, *Nano Res.* **2010**, *3*, 117.

[16] a) P. Doppelt, G. Hallais, J. Pinson, F. Podvorica, S. Verneyre, *Chem. Mater.* **2007**, *19*, 4570; b) V. Rebuttini, E. Fazio, S. Santangelo, F. Neri, G. Caputo, C. Martin, T. Brousse, F. Favier, N. Pinna, *Chem. – Eur. J.* **2015**, *21*, 12465; c) M. Toupin, D. Bélanger, *Langmuir* **2008**, *24*, 1910; d) S. Q. Lud, M. Steenackers, R. Jordan, P. Bruno, D. M. Gruen, P. Feulner, J. A. Garrido, M. Stutzmann, *J. Am. Chem. Soc.* **2006**, *128*, 16884; e) S. Betelu, I. Tijunelyte, L. Boubekeur-Lecaque, I. Ignatiadis, J. Ibrahim, S. Gaboreau, C. Berho, T. Toury, E. Guenin, N. Lidgi-Guigui, N. Félidj, E. Rinnert, M. L. d. l. Chapelle, *J. Phys. Chem. C* **2016**, *120*, 18158.

[17] a) F. M. Koehler, A. Jacobsen, K. Ensslin, C. Stampfer, W. J. Stark, *Small* **2010**, *6*, 1125; b) D. B. Farmer, R. Golizadeh-Mojarad, V. Perebeinos, Y.-M. Lin, G. S. Tulevski, J. C. Tsang, P. Avouris, *Nano Lett.* **2009**, *9*, 388.

[18] a) G. L. C. Paulus, Q. H. Wang, M. S. Strano, *Acc. Chem. Res.* **2013**, *46*, 160; b) M. Quintana, A. Montellano, A. E. del Rio Castillo, G. V. Tendeloo, C. Bittencourt, M. Prato, *Chem. Commun.* **2011**, *47*, 9330.

[19] a) P. Tan, S. Dimovski, Y. Gogotsi, *Philos. Trans. R. Soc., A* **2004**, *362*, 2289; b) M. S. Dresselhaus, A. Jorio, A. G. Souza Filho, R. Saito, *Philos. Trans. R. Soc., A* **2010**, *368*, 5355.

[20] M. S. Dresselhaus, A. Jorio, R. Saito, *Annu. Rev. Condens. Matter Phys.* **2010**, *1*, 89.

[21] R. Saito, A. Jorio, A. G. Souza Filho, G. Dresselhaus, M. S. Dresselhaus, M. A. Pimenta, *Phys. Rev. Lett.* **2001**, *88*, 027401.

[22] a) A. C. Ferrari, J. Robertson, *Phys. Rev. B* **2001**, *63*, 121405; b) A. C. Ferrari, J. Robertson, *Philos. Trans. R. Soc., A* **2004**, *362*, 2477.

[23] S. Lefrant, L. S. Lichtmann, H. Temkin, D. B. Fitchen, D. C. Miller, G. E. Whitwell, J. M. Burlitch, *Solid State Commun.* **1979**, *29*, 191.

[24] W. Ren, R. Saito, L. Gao, F. Zheng, Z. Wu, B. Liu, M. Furukawa, J. Zhao, Z. Chen, H.-M. Cheng, *Phys. Rev. B* **2010**, *81*, 035412.

[25] I.-Y. Jeon, Y.-R. Shin, G.-J. Sohn, H.-J. Choi, S.-Y. Bae, J. Mahmood, S.-M. Jung, J.-M. Seo, M.-J. Kim, D. Wook Chang, L. Dai, J.-B. Baek, *Proc. Natl. Acad. Sci. USA* **2012**, *109*, 5588.

[26] J. M. Englert, C. Dotzer, G. Yang, M. Schmid, C. Papp, J. M. Gottfried, H.-P. Steinrück, E. Spiecker, F. Hauke, A. Hirsch, *Nat. Chem.* **2011**, *3*, 279.

[27] a) G. Socrates, *Infrared and Raman Characteristic Group Frequencies: Tables and Charts*, J. Wiley & Sons, West Sussex, UK **2001**; b) G. Rajender, P. K. Giri, *J. Mater. Chem. C* **2016**, *4*, 10852.
[28] a) R. S. Chellappa, D. M. Dattelbaum, J. D. Coe, N. Velisavljevic, L. L. Stevens, Z. Liu, *J. Phys. Chem. A* **2014**, *118*, 5969; b) Y.-F. Huang, H.-P. Zhu, G.-K. Liu, D.-Y. Wu, B. Ren, Z.-Q. Tian, *J. Am. Chem. Soc.* **2010**, *132*, 9244.
[29] a) K. W. Putz, O. C. Compton, C. Segar, Z. An, S. T. Nguyen, L. C. Brinson, *ACS Nano* **2011**, *5*, 6601; b) P. Sheath, M. Majumder, *Philos. Trans. R. Soc., A* **2016**, *374*, 20150028.
[30] L. Paliotta, G. De Bellis, A. Tamburrano, F. Marra, A. Rinaldi, S. K. Balijepalli, S. Kaciulis, M. S. Sarto, *Carbon* **2015**, *89*, 260.
[31] S. Doniach, M. Sunjic, *J. Phys. C: Solid State Phys.* **1970**, *3*, 285.
[32] a) A. Ganguly, S. Sharma, P. Papakonstantinou, J. Hamilton, *J. Phys. Chem. C* **2011**, *115*, 17009; b) E. Bekyarova, M. E. Itkis, P. Ramesh, C. Berger, M. Sprinkle, W. A. de Heer, R. C. Haddon, *J. Am. Chem. Soc.* **2009**, *131*, 1336.
[33] H. Sun, *J. Phys. Chem. B* **1998**, *102*, 7338.
[34] A. K. Rappe, W. A. Goddard, *J. Phys. Chem.* **1991**, *95*, 3358.
[35] S. Ghosh, W. Bao, D. L. Nika, S. Subrina, E. P. Pokatilov, C. N. Lau, A. A. Balandin, *Nat. Mater.* **2010**, *9*, 555.
[36] B. Mortazavi, T. Rabczuk, *Carbon* **2015**, *85*, 1.